POD-based study of structure and dynamics in turbulent plane Poiseuille flow: comparing quasi-linear simulations to DNS

Marios-Andreas Nikolaidis[1]†, Petros J. Ioannou[1,2], Brian F. Farrell[2], Adrián Lozano-Durán[3]

[1]Department of Physics, National and Kapodistrian University of Athens, Athens, Greece

[2]Department of Earth and Planetary Sciences, Harvard University, Cambridge, U.S.A.

[3]Department of Aeronautics and Astronautics, Massachusetts Institute of Technology, Cambridge, U.S.A.

(Received xx; revised xx; accepted xx)

Turbulence structure in the quasi-linear restricted nonlinear (RNL) model is analyzed and compared with DNS of turbulent Poiseuille flow at Reynolds number $R = 1650$. The turbulence structure is obtained by POD analysis of the two components of the flow partition used in formulating the RNL model: the streamwise-mean flow and the associated perturbations. The dominant structures are found to be similar in RNL simulations and DNS despite the neglect of perturbation-perturbation nonlinearity in the RNL formulation. POD analysis of the streamwise-mean flow indicates that the dominant structure in both RNL and DNS is a coherent roll-streak structure in which the roll is collocated with the streak in a manner configured to reinforce the streak by the lift-up process. This mechanism of roll-streak maintenance accords with analytical predictions made using the second order statistical state dynamics (SSD) model, referred to as S3T, which shares with RNL the dynamical restriction of neglecting the perturbation-perturbation nonlinearity. POD analysis of perturbations from the streamwise-mean streak reveals that similar structures characterize these perturbations in both RNL and DNS. The perturbation to the low-speed streak POD are shown to have the form of oblique waves collocated with the streak that can be identified with optimally growing structures on the streak. Given that the mechanism sustaining turbulence in RNL has been analytically characterized, this close correspondence between the streamwise-mean and perturbation structures in RNL and DNS supports the conclusion that the self-sustaining mechanism in DNS is the same as that in RNL. This mechanism has been shown by analysis of the closely related S3T SSD and its RNL approximation to be characterized by Reynolds stresses arising from the transient development of oblique waves. These oblique waves arise in RNL as Lyapunov modes on the streak which are closely related to optimally growing structures on the streak and properly collocated with the streak to induce streamwise torque driving of the roll circulations required to produce lift-up forcing of the streamwise streak.

Key words:

---

† Email address for correspondence: mnikolaidis@phys.uoa.gr

1. Introduction

The Proper Orthogonal Decomposition (POD) (Lumley 1967; Aubry *et al.* 1988; Moin & Moser 1989; Berkooz *et al.* 1993; Sirovich *et al.* 1990; Moehlis *et al.* 2002; Hellström *et al.* 2011; Hellström & Smits 2017) provides an orthonormal basis for the spatial structure of a time-dependent velocity field that is optimally configured in the sense that the components are ordered according to their contribution to variance. In order to diagnose the dynamical mechanism supporting turbulence in plane Poisseuille flow, two sets of POD modes are obtained from turbulence in a DNS and in the associated restricted nonlinear (RNL) model. These POD sets are chosen to correspond to the two components of the second order statistical state dynamics (SSD) referred to as S3T for which analytical solution for the closure of turbulence has been obtained (Farrell & Ioannou 2012; Farrell *et al.* 2017*a*). The RNL model is dynamically similar to the S3T SSD and provides a close approximation to the S3T SSD model so that comparison of these sets of POD modes allows us to diagnose how close the dynamics of DNS is to that of RNL and therefore to the dynamics identified in the analytical S3T closure. To this end, in this work we obtain the POD modes for deviations of the streamwise-mean flow from its temporal and spanwise-mean, for which the streamwise wavenumber is $k_x = 0$, and for deviations from the streamwise-mean streak, for which the streamwise wavenumber is $k_x \neq 0$, in both the turbulence of the DNS and in the turbulence of the associated RNL model.

The dynamics of RNL turbulence is restricted by neglecting the nonlinear interaction among perturbations from the streamwise-mean flow. Despite the substantial simplification of the dynamics resulting from neglecting perturbation-perturbation nonlinearity in the perturbation equation, this quasi-linear RNL system maintains a turbulent state. Moreover, RNL turbulence undergoes spontaneous decrease in the number of streamwise harmonics supported by the turbulence, to as few as a single harmonic. Despite this great spontaneously occurring simplification of RNL dynamics and its quasi-linear form, many of the salient features of DNS turbulence are also seen in RNL turbulence (Thomas *et al.* 2014, 2015; Bretheim *et al.* 2015; Farrell *et al.* 2016, 2017*a*). This compelling similarity between RNL and DNS turbulence strongly suggests that these turbulent states are sustained by the same mechanism. While the mechanism sustaining DNS turbulence continues to be debated (Jiménez & Moin 1991; Hamilton *et al.* 1995; Waleffe 1997; Jiménez & Pinelli 1999; Kawahara & Kida 2001; Schoppa & Hussain 2002; Waleffe 2003; Chernyshenko & Baig 2005; Hwang & Cossu 2010, 2011; Hwang *et al.* 2016; Lozano-Durán *et al.* 2021), RNL turbulence self-sustains by a completely characterized interaction between the time-dependent streamwise-mean roll-streak and the streamwise-varying flow component. The mechanism maintaining the perturbations in RNL turbulence is linear non-normal parametrically sustained transfer of energy from the fluctuating mean flow to the perturbation field. This transfer is effected by the Lyapunov vectors supported by the fluctuating mean flow and specifically the small set of Lyapunov vectors with zero Lyapunov exponent. This small set of Lyapunov vectors comprise the entire support of the perturbation variance in RNL turbulence. While the mean flow is maintaining the perturbation variance by transferring energy to these Lyapunov vectors, the Reynolds stresses resulting from these perturbations are maintaining the fluctuation of the mean flow. The resulting synergistic loop comprises the mechanism supporting the turbulent state: fluctuation of the mean flow is supported by its interaction with the perturbations, while the fluctuating mean flow provides the parametric growth mechanism by which the perturbation variance is sustained (Farrell & Ioannou 2012, 2017; Farrell *et al.* 2018). Completing comprehensive analytical characterization of S3T-RNL turbulence is identification of the mechanism regulating the turbulence to its observed statistical

mean state. This mechanism is identified in the dynamically similar S3T-RNL systems as feedback on the streamwise-mean roll-streak by the Lyapunov-induced perturbation Reynolds stress which regulates the roll-streak to maintain precisely zero perturbation Lyapunov exponents for the supporting perturbation structures (Farrell & Ioannou 2012, 2017; Farrell *et al.* 2018). The compelling similarity of DNS and RNL turbulence argues that the same dynamics, which has comprehensive analytical characterization in RNL, is responsible also for the turbulence in DNS. Given the implications of this identification for theoretical understanding of turbulence it is important to examine its validity. In this work structure and mechanism diagnostics obtained by POD analysis of RNL and DNS turbulence are shown to provide compelling evidence for identifying the analytically characterized mechanism supporting RNL turbulence with that supporting DNS turbulence.

2. DNS and its RNL approximation

We choose to study a pressure driven constant mass-flux plane Poiseuille flow in a channel which is doubly periodic in the streamwise, x, and spanwise, z, direction. We decompose the incompressible non-dimensional Navier-Stokes equations governing the channel flow into equations for the streamwise mean flow, $\mathbf{U}$, and the perturbations, $\mathbf{u}$, as follows:

$$\partial_t \mathbf{U} + \mathbf{U}\cdot\nabla\mathbf{U} - G(t)\hat{\mathbf{x}} + \nabla P - R^{-1}\Delta\mathbf{U} = -\overline{\mathbf{u}\cdot\nabla\mathbf{u}}\ , \tag{2.1a}$$

$$\partial_t \mathbf{u} + \mathbf{U}\cdot\nabla\mathbf{u} + \mathbf{u}\cdot\nabla\mathbf{U} + \nabla p - R^{-1}\Delta\mathbf{u} = -(\mathbf{u}\cdot\nabla\mathbf{u} - \overline{\mathbf{u}\cdot\nabla\mathbf{u}})\ . \tag{2.1b}$$

$$\nabla\cdot\mathbf{U} = 0\ , \quad \nabla\cdot\mathbf{u} = 0\ . \tag{2.1c}$$

No-slip and impermeable boundaries are placed at $y = 0$ and $y = 2$, in the wall-normal variable. The pressure gradient $G(t)$ is adjusted in time to maintain constant mass flux. An overline, e.g. $\overline{\mathbf{u}\cdot\nabla\mathbf{u}}$, denotes averaging in x. Capital letters indicate streamwise averaged quantities. Lengths have been made nondimensional by h, the channel's half-width, velocities by $\langle U\rangle_c$, the center velocity of the time-mean flow, and time by $h/\langle U\rangle_c$. The Reynolds number is $R = \langle U\rangle_c h/\nu$, with ν the kinematic viscosity.

The corresponding RNL equations are obtained by suppressing nonlinear interactions among streamwise non-constant flow components in the perturbation equations resulting in the right hand side of (2.1*b*) being neglected. The RNL equations are:

$$\partial_t \mathbf{U} + \mathbf{U}\cdot\nabla\mathbf{U} - G(t)\hat{\mathbf{x}} + \nabla P - R^{-1}\Delta\mathbf{U} = -\overline{\mathbf{u}\cdot\nabla\mathbf{u}}\ , \tag{2.2a}$$

$$\partial_t \mathbf{u} + \mathbf{U}\cdot\nabla\mathbf{u} + \mathbf{u}\cdot\nabla\mathbf{U} + \nabla p - R^{-1}\Delta\mathbf{u} = 0\ . \tag{2.2b}$$

$$\nabla\cdot\mathbf{U} = 0\ , \quad \nabla\cdot\mathbf{u} = 0\ . \tag{2.2c}$$

Under this quasi-linear restriction, the perturbation field interacts nonlinearly only with the mean, $\mathbf{U}$, flow and not with itself. This quasi-linear restriction of the dynamics results in the spontaneous collapse in the support of the perturbation dynamics to a small subset of streamwise Fourier components. It is important to recognize that this restriction in the support of the RNL turbulence to a small subset of streamwise Fourier components is not imposed but rather is a property of the dynamics with significant implication. The components that are retained by the RNL dynamics identify the streamwise harmonics that are dynamically active in the sense that this subset of streamwise harmonics is energetically active in the parametric instability that sustains the perturbation component of the turbulent state (Farrell & Ioannou 2012; Thomas *et al.* 2014, 2015; Farrell *et al.* 2016) and are responsible in DNS, in which all the streamwise components are supported, for synchronization of the remaining components (Nikolaidis & Ioannou 2021).

Abbreviation	$[L_x, L_y, L_z]$	$[L_x^+, L_y^+, L_z^+]$	$N_x \times N_z \times N_y$	R_τ	R
NL100	$[4\pi\ ,\ 2\ ,\ \pi]$	[1264 , 201 ,316]	$128 \times 63 \times 97$	100.59	1650
RNL100	$[4\pi\ ,\ 2\ ,\ \pi]$	[1171 , 186 ,293]	$16 \times 63 \times 97$	93.18	1650

Table 1: Simulation parameters. $[L_x, L_y, L_z]/h$, where h is the channel half-width, is the domain size in the streamwise, wall-normal and spanwise direction. Similarly, $[L_x^+, L_y^+, L_z^+]$, indicates the domain size in wall-units. N_x, N_z are the number of Fourier components after dealiasing and N_y is the number of Chebyshev components. $R_\tau = u_\tau h/\nu$ is the Reynolds number of the simulation based on the friction velocity $u_\tau = \sqrt{\nu\, \mathrm{d}\langle U\rangle/\mathrm{d}y|_{\mathrm{w}}}$,where $\mathrm{d}\langle U\rangle/\mathrm{d}y|_{\mathrm{w}}$ is the shear at the wall.

The data were obtained from a DNS of Eq. (2.1) and from the associated RNL governed by Eq. (2.2). The Reynolds number $R = \langle U\rangle_c h/\nu = 1650$ is imposed in both the DNS and the RNL simulations. A summary of the parameters of the simulations is given in Table 1. The time averaged streamwise mean flow $\langle U\rangle$ and its associated shear in the DNS and RNL simulation are shown in Fig. 1 and the time-averaged rms profiles of the fluctuations from the mean flow $\langle U\rangle$, $\mathbf{u}' = \mathbf{u} - \langle U\rangle$, are shown in Fig. 2 The RNL simulation reported here is supported by only three streamwise components with wavelengths $\lambda_x/h = 4\pi, 2\pi, 4\pi/3$, which correspond to the three gravest streamwise Fourier components of the channel, $n_x = 1, 2, 3$.

For the numerical integration the dynamics were expressed in the form of evolution equations for the wall-normal vorticity and the Laplacian of the wall-normal velocity, with spatial discretization and Fourier dealiasing in the two wall-parallel directions and Chebychev polynomials in the wall-normal direction (Kim *et al.* 1987). Time stepping was implemented using the third-order semi-implicit Runge-Kutta method.

3. Analysis method used in obtaining the POD modes

POD analysis requires the two-point same-time spatial covariance of the flow-field variables. The perspective on turbulence dynamics adopted in this work is that of the S3T SSD and its RNL approximation. The insights of this SSD proceed from its formulation which is based on using the streamwise-mean and associated perturbations to express the dynamics. The dominant coherent structure supporting turbulence in the S3T SSD is the roll-streak. In order to further isolate this structure the analysis is confined to deviations of the streamwise mean flow from its spanwise mean. Adopting the notation $\langle\, \cdot\, \rangle$ for the time average , $[\, \cdot\,]$ for the spanwise average, and $(\, \cdot\,)^T$ for transposition, the covariance of deviations of the streamwise-mean velocity field from its spanwise-mean is:

$$C = \langle \mathcal{U}\mathcal{U}^T \rangle \ , \tag{3.1}$$

in which

$$\mathcal{U} = [U_s, V_s, W_s]^T \ , \tag{3.2}$$

is the column vector comprised of the deviations of the three streamwise mean components from their spanwise-mean, $([U](y,t), [V](y,t), [W](y,t))$, i.e. $U_s = U - [U]$, $V_s = V - [V]$, and $W_s = W - [W]$. A requirement for $\mathcal{C}$ to be a covariance is that $\langle U_s\rangle = 0$, $\langle V_s\rangle = 0$ and $\langle W_s\rangle = 0$, which demands that $\langle [U]\rangle = \langle U\rangle$, $\langle [V]\rangle = \langle V\rangle$ and $\langle [W]\rangle = \langle W\rangle$. This condition places a requirement of homogeneity on the velocity components in z, which was verified.

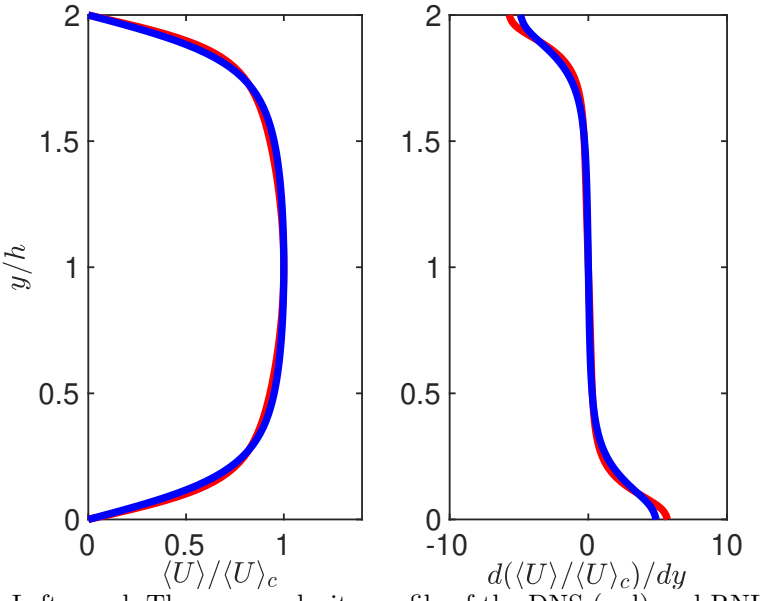

Figure 1: Left panel: The mean velocity profile of the DNS (red) and RNL simulations (blue) normalized to the average centerline velocity $\langle U \rangle_c$. Right panel: The corresponding normalized mean shear in the two simulations.

The dominant structures in the S3T SSD perturbation field are associated with the streamwise streak. In order to isolate these structures the perturbations are obtained by first collocating the dominant streak together with its associated perturbation field in the flow prior to extracting the perturbations from the dominant streak. These perturbations are used to form the covariance on which the POD analysis is done, as described in section 5. The covariance of the perturbation flow field is expressed as:

$$c = \left\langle \mathcal{U}' \mathcal{U}'^{\mathcal{T}} \right\rangle, \tag{3.3}$$

with

$$\mathcal{U}' = [u, v, w]^T, \tag{3.4}$$

the column vector of the three velocity components of the streamwise varying flow (the components of the perturbation velocity) from the collocated dominant streak structure in the flow.

The POD basis for the mean flow perturbations and for the perturbations from the dominant streak are obtained by eigenanalysis of the two-point covariances, C and c. The resulting orthonormal set of eigenvectors is then ordered descending in eigenvalue to form these POD bases. The eigenvalue of each POD is its time-averaged contribution to the variance of the velocity.

To obtain a converged POD basis for the streamwise mean flow a long time series of the turbulent flow field is required. Convergence is also facilitated by taking into account the statistical symmetries of the flow: homogeneity in the x and z direction, mirror symmetry in y about the $x-z$ plane at the channel center, and mirror symmetry in z about the $y-x$ plane at the channel center in the spanwise direction. Details of the implementation of the symmetries for the calculation of the POD's are given in Appendix A. As the averaging time increases statistics of flow quantities have been verified to approach asymptotically these symmetries. These statistical symmetries are not necessary consequences of the

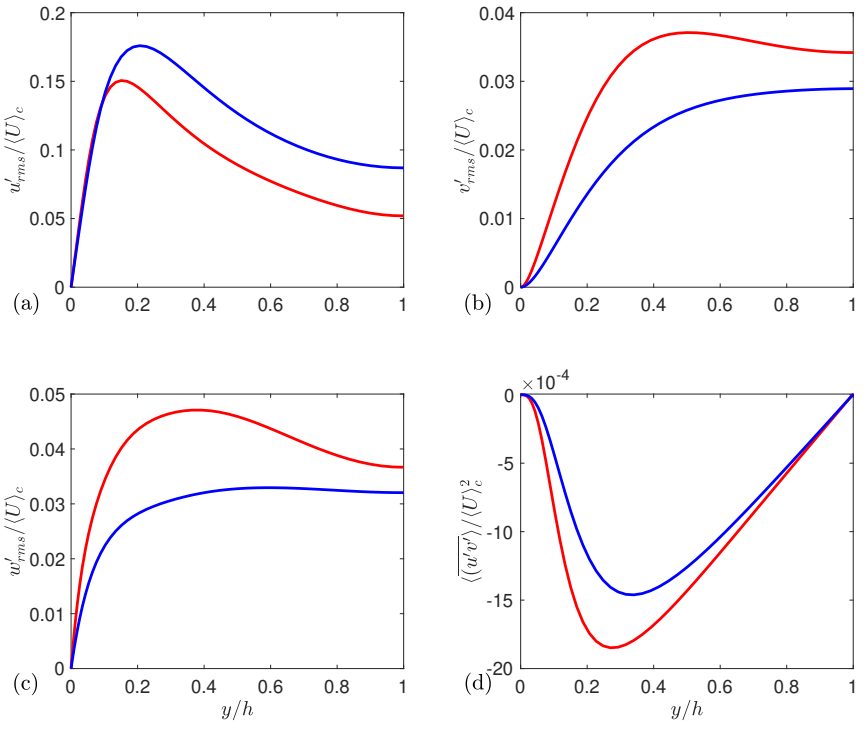

Figure 2: Wall-normal profiles of the rms of velocity fluctuations (a,b,c) and the tangential Reynolds stress (d) for the DNS (red) and RNL (blue) simulations.

translation and mirror symmetry of the NS equations in a periodic channel because the solutions may undergo symmetry breaking. For example stability analysis of the S3T SSD of wall-bounded flows in periodic domains predicts symmetry breaking of spanwise homogeneity before the turbulent state is established (Farrell & Ioannou 2012; Farrell *et al.* 2017*b*). Persistent symmetry breaking in pipe flow is also revealed by a turbulent state with temporally constant and spatially fixed streak structures aligned parallel to the streamwise axis that are for practical purposes invariant (cf. Avsarkisov *et al.* (2014)).

The POD modes provide an optimally compact basis to reconstruct the perturbation velocity field and in that sense provide an optimal basis for comparing flow structure. For example, Aubry *et al.* (1988) using POD analysis on experimental data were able to identify the roll-streak structure and Sirovich *et al.* (1990) using DNS data identified this structure in the near-wall region. More recently, Hellström & Smits (2017) in a series of papers using POD analysis on experimental data from the Princeton super-pipe and also from DNS elucidated the structure of the very large scale roll-streaks (VLSM) in the outer layer. It should be kept in mind that although the POD basis is optimally compact for representing perturbation variance, this basis is not optimally compact for representing dynamics of fluid flow, which requires, because of the high non-normality of the perturbation growth processes, information on the energy optimals that have low amplitude and complex structure and consequently are in practice unobservable (for a discussion of the relation of the POD basis to the dynamics refer to Farrell & Ioannou

(1993); construction of a basis for optimal representation of flow dynamics using balanced truncations is described in Farrell & Ioannou (2001); Rowley (2005)). However, the POD basis does identify the unique structure containing the maximum average variance for a given norm (the first POD) and provides a basis systematically identifying the hierarchy of subspaces within which the variance is supported, which has dynamical significance. For instance, a theory for maintenance of the perturbation field should predict this ordering of the subspaces supporting the perturbation variance.

4. POD modes of the DNS and RNL streamwise mean flow

The POD basis for the $k_x = 0$ component of the deviations from the time and spanwise mean velocity in the DNS and the RNL simulation will now be described. Statistical homogeneity in z implies that the eigenvectors of C, which are the POD's, are single Fourier harmonics in the spanwise direction with wavenumber k_z of the form:

$$\Phi_{k_z} = \begin{pmatrix} A_{k_z}(y) \\ B_{k_z}(y) \\ \Gamma_{k_z}(y) \end{pmatrix} e^{ik_z z} , \tag{4.1}$$

where $A_{k_z}(y)$ is the streamwise component of the velocity field associated with the POD, $B_{k_z}(y)$ the wall-normal and $\Gamma_{k_z}(y)$ the spanwise component. All these components are specified as N_y dimensional column vectors, with N_y the number of discretization points in y (Berkooz *et al.* 1993). At each sampling time the $3N_y$ column vector of a $k_z \neq 0$ Fourier component, $\mathcal{U}_{k_z}(t)$, of the flow field $\mathcal{U}$ is obtained and used to form N_{k_z} average covariances:

$$C_{k_z} = \left\langle \mathcal{U}_{k_z}(t)\mathcal{U}^{\dagger}_{k_z}(t) \right\rangle , \tag{4.2}$$

where N_{k_z} is the number of $k_z \neq 0$ Fourier components retained in the simulation and $\dagger$ is the Hermitian transpose. Eigenanalysis of these covariances determines $3N_y \times N_{k_z}$ eigenvectors comprising the POD orthonormal basis of the $k_x = 0$ flow field taking into account the restriction to deviations from the spanwise mean mentioned above. These POD's are ordered decreasing in eigenvalue which corresponds to variance.

As discussed above, because of the statistical homogeneity of the flow in the z direction, the $k_x = 0$ POD modes come in $\sin(k_z z)$ and $\cos(k_z z)$ pairs. One of each pair of the first 6 POD modes of the DNS simulation is shown in Fig. 3 and the corresponding POD modes for the RNL simulation in Fig. 4. Shown are both the streak velocity and the corresponding (V_s, W_s) velocity field for each POD. Note that both the DNS and the RNL simulation exhibit POD modes indicating the streamwise velocity is collocated with similar roll-streak structures. The percentage variance explained by the first POD modes is also similar in the DNS and RNL simulation as shown in Fig. 5.

Of dynamical significance is the systematic correlation between the wall-normal velocity V_s of the roll and the corresponding streak velocity in these POD modes: positive V_s is correlated with low speed streaks (defects in the streamwise average flow) and vice versa in all the POD modes. That all the POD modes exhibit this correlation is consistent with the interpretation that the rolls and the streaks form a coherent structure in which the lift-up mechanism arising from the roll is acting to maintain the streak. If instead the streaks were maintained directly by e.g. Reynolds stress forcing from the perturbation field then no such systematic correlation between roll velocities and streak velocities would be expected. Consistently, previous work has revealed that the Reynolds stress resulting from streak-induced organization of turbulence in S3T/RNL results in maintenance of a lift-up process supporting roll-streaks with the same structure as these POD's. Also consistent is

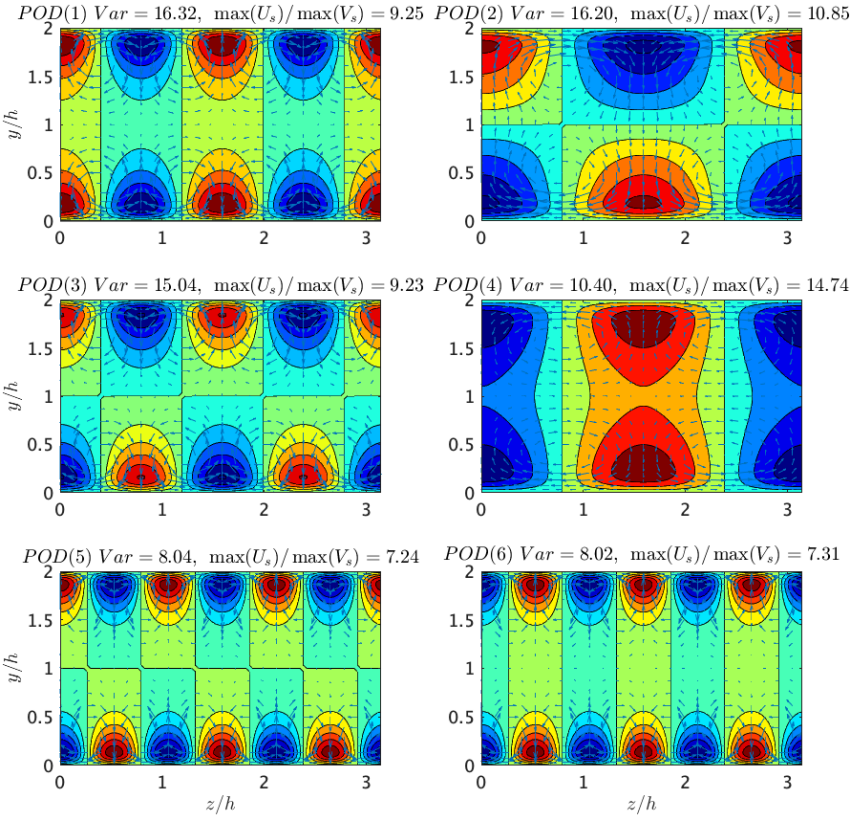

Figure 3: The first 6 POD modes of the streamwise-mean flow from a 310000 advective time units DNS. The contours show levels of the streamwise U_s velocity and the arrows show the cross stream-spanwise velocity vector (V_s, W_s).

that the roll-streak is shown in these analyses to be maintained by the lift-up mechanism while the perturbation Reynolds stresses oppose the streak rather than maintain it (Farrell & Ioannou 2012; Farrell *et al.* 2016). Note that the first 6 DNS POD modes with $k_x = 0$ have roll-streak structure nearly identical to those in the RNL model, albeit with some reordering. The velocity variance of the primary POD differs in the DNS and the RNL as would be expected given that the RNL is supported by only three streamwise-varying wavenumbers, of which one is dominant. This similarity of the RNL and DNS streamwise-mean POD modes suggests strongly that the same dynamics is operating. In the case of RNL this dynamics is known to be that the streaks organize the perturbations so that their associated Reynolds stresses produce streamwie torque configured to force rolls collocated with the streak in such a manner as to reinforce the preexisting streak by the lift-up process. This reinforcement mechanism is persuasively manifest in the idealized problem of the instability of a background of spanwise homogeneous turbulence to the formation of streamwise streaks. Statistical state dynamics calculations closed at second order identify this instability, which is the fundamental instability underlying the dynamics of turbulence in shear flow, by showing that the roll/streak structure is the

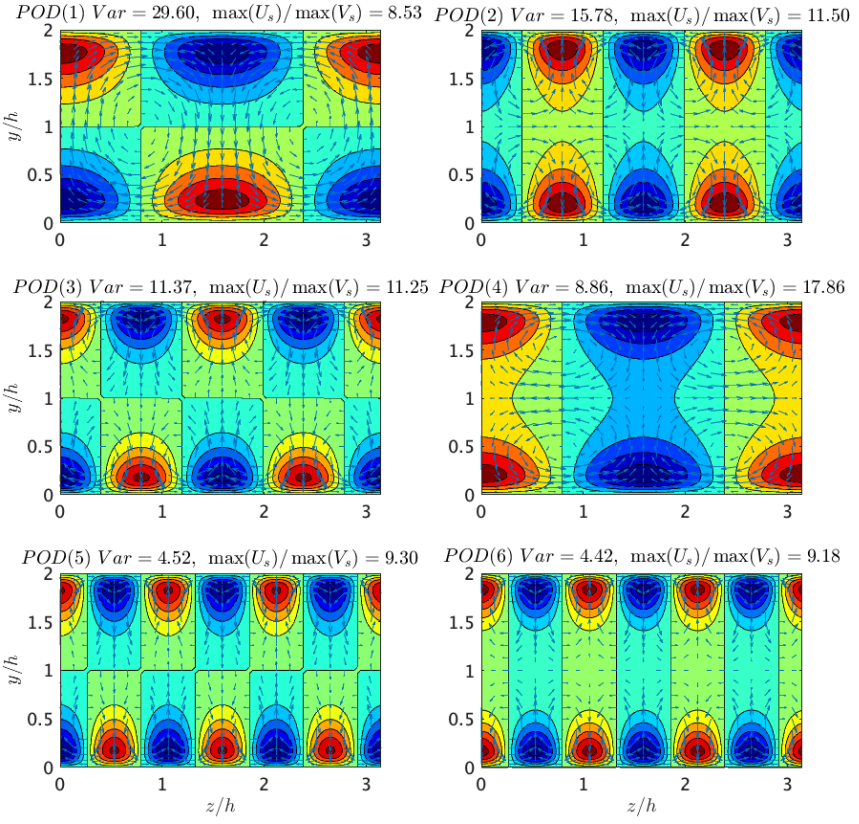

Figure 4: The first 6 POD modes of the streamwise-mean flow from a 83000 advective time units simulation of RNL turbulence corresponding to the DNS shown in Fig. 3. The contours show levels of the streamwise U_s velocity and the arrows show the cross stream-spanwise velocity vector (V_s, W_s).

dominant unstable eigenfunction in the SSD. Moreover, this unstable eigenfunction has the same form as the POD we have identified in RNL and DNS.

The wall-normal velocities of the roll component of the POD modes are about 1/10 the streak velocity which, assuming an average non-dimensional mean flow shear of magnitude 2 (cf. Fig. 1) is consistent with the emergence of the associated streak through the lift-up mechanism over 5 time units.

5. POD modes of the streamwise-varying perturbations from the dominant streak occurring in flow realizations

A fundamental dynamical property of turbulence in wall-bounded flows is the spontaneous breaking of the spanwise symmetry by the formation of the roll-streak structure. Although there is no instability associated with this symmetry breaking in the traditional formulation of the NS using velocity components for the state, this symmetry is broken by the most unstable mode of the simplest nontrivial SSD which is a cumulant expansion closed at second order using streamwise-mean velocity and perturbation covariance for

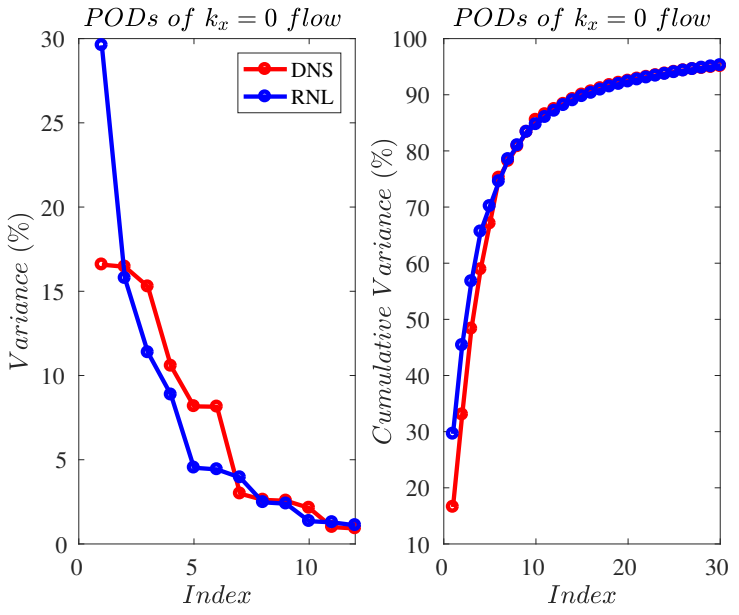

Figure 5: Left panel: Percentage variance of the streamwise-mean ($k_x = 0$) flow explained by each POD doublet in the DNS and RNL simulation. Right panel: The cumulative variance accounted for by the POD modes in the DNS and RNL simulation as a function of the number of POD modes included in the sum.

the state variables (Farrell & Ioannou 2012). While the underlying roll-streak symmetry breaking instability is analytic in pre-transitional flow analyses made using the S3T SSD (Farrell *et al.* 2017*b*), the manifestation of this symmetry breaking instability is made imperfect by time dependence both in the pre-transitonal and post-transitional DNS and RNL solutions so that the roll-streak structure, while prominent, is randomly spatially displaced rather than persisting at a fixed spanwise location. Nevertheless, the existence of the underlying symmetry break in the spanwise by the roll-streak S3T instability is clearly manifest in the substantial spatial extent in the steamwise direction and persistence in time of the roll-streak structure in RNL and DNS, indicative of the analytical underlying bifurcation. Informed by the existence of an analytic bifurcation to a time and space independent roll-streak structure in pre-transitional flow, we wish to isolate structures underlying this fundamental mechanism of roll-streak maintenance from the secondary property of variation of the streak location in the spanwise direction. By this simplification we are able to concentrate on the interaction of the roll-steak with streamwise perturbations, which is widely recognized to be associated with the maintenance of turbulence, although the dynamics of this interaction remains controversial (cf. Jiménez & Moin (1991); Hamilton *et al.* (1995); Waleffe (1997); Jiménez & Pinelli (1999); Schoppa & Hussain (2002); Farrell & Ioannou (2012, 2017); Farrell *et al.* (2017*a*)). A point of agreement of the above studies is that the streak and perturbations are collocated to form a self-reinforcing dynamical structure. Thus, an accurate statistical description of the $k_x \neq 0$ structures will be sought by performing at every instant of time a spanwise translation of the entire flow field data so that the dominant streak together with its associated perturbations is at the center of the channel, $z/h = \pi/2$.

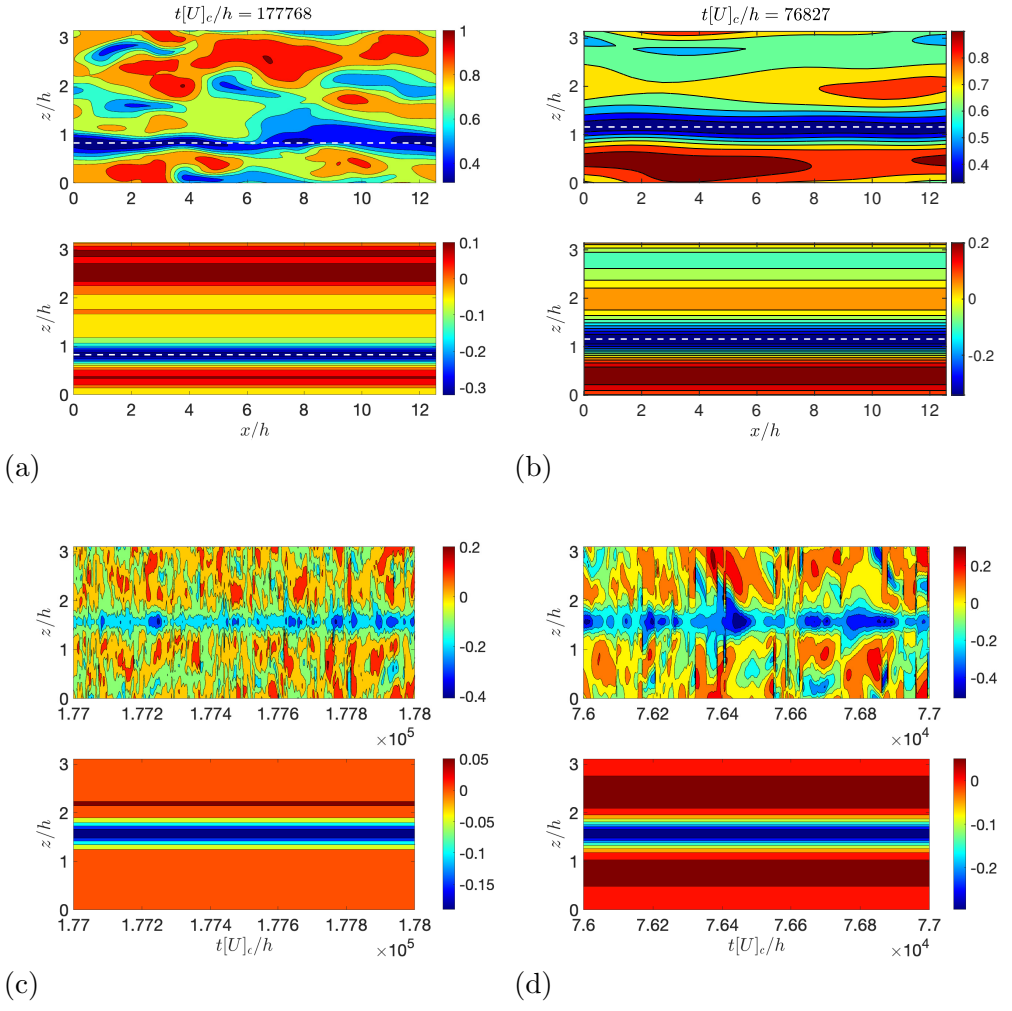

Figure 6: (a) Top panel: A snapshot of the streamwise velocity u at $t[U]_c/h = 177768$ from the NL100 simulation at the wall-normal plane $y/h = 0.21$. Bottom panel: The U_s component of the above snapshot. The white dashed line in both figures indicates the spanwise location of the U_s minimum. (b) Same as (a) for a snapshot of the RNL100 at $t[U]_c/h = 76827$. (c) Top panel: A temporal sequence of U_s snapshots for which the streak minima have been aligned at the channel half-width $z/h = \pi/2$. The total flow snapshot is also subjected to the same shift. Bottom panel: The ensemble average U_s converges to a negative central streak region with weak positive regions on its flanks, whereas the remaining flow is almost spanwise homogeneous. (d) Same as (c) for the ensemble average U_s of the RNL100 simulation.

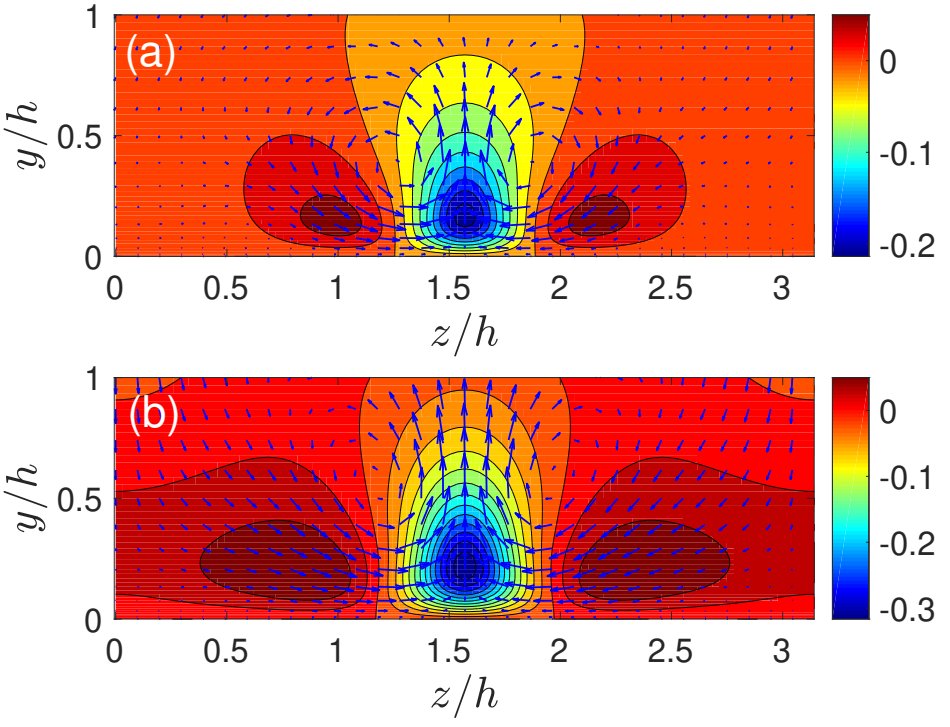

Figure 7: Contours of the time average collocated U_s and vectors of the roll (W_s, V_s) velocity on the (z, y) plane for the NS100 (panel(a)) and RNL100 (panel (b)). The contour level step is 0.025 in both panels. Panel (a): $\max(|U_s|) = 0.21$, $\max(V_s) = 0.024$. Panel (b): $\max(|U_s|) = 0.32$, $\max(V_s) = 0.03$.

A reliable indicator of the streak location is the spanwise z/h coordinate of the $\min(U_s)$ associated with the dominant low speed streak structure (Figs. 6a and 6b). We proceed to identify this location in the flow realizations by finding the z coordinate of this minimum velocity at a fixed distance from the wall, $y/h = 0.21$, where the $|\min(U_s)|$ attains it's largest values, and translate the total flow field so that the U_s minima occur at the same spanwise location at the center of the channel at $z/h = \pi/2$, while retaining the time order. The effect of this operation on the streamwise average U_s velocity is shown in the top panel of Figs. 6c and 6d for NL100 and RNL100 respectively. The modified time-series of the U_s produce an aligned slow speed region at $z/h = \pi/2$ in both cases, while further away from this core region the uncorrelated high and low speed streaks cancel out. The streamwise-mean streak, U_s, on the plane $y/h = 0.21$ resulting from this procedure is shown in the bottom panel of Figs. 6c and 6d. The structure in the $y - z$ plane of the roll-streak for NL100 and RNL100 is shown in Figs. 7a,b using contours for U_s and vectors for (W_s, V_s). Note that asymptotically the roll-streak structure becomes symmetric about the center of the streak consistent with the flow being spanwise mirror symmetric.

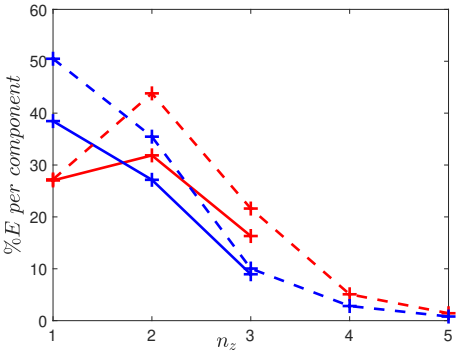

Figure 8: The percentage energy accounted for by the first spanwise Fourier components of the mean streaks in Fig. 7. Dashed red line: for the mean streak of the DNS, dashed blue line: for the mean streak of the RNL. The solid lines with the corresponding colors show the percentage energy of the corresponding POD's.

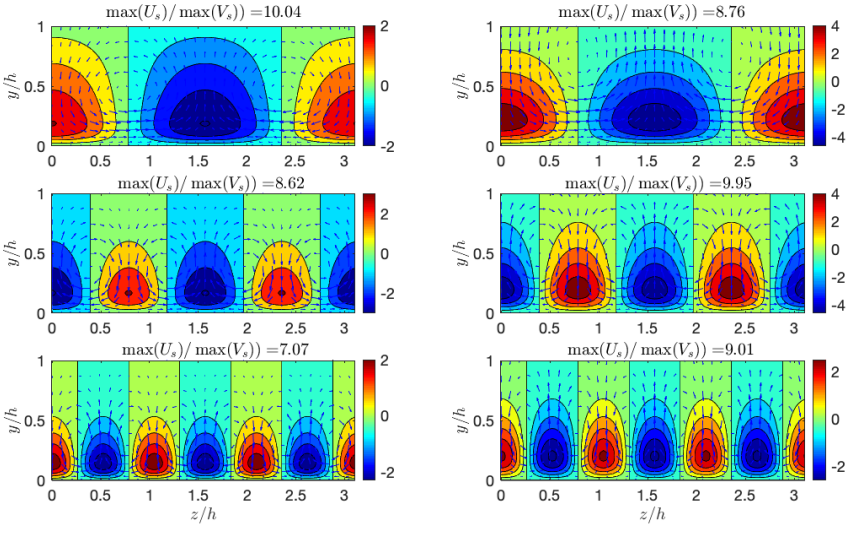

Figure 9: Contours of the U_s and vectors of the roll (W_s, V_s) velocity on the (z, y) plane of the first three spanwise Fourier components of the mean streaks of Fig. 7. Left column of the DNS, right column of the RNL. The contour level step is 0.5 in all panels.

5.1. *Relating POD modes to roll-streak structures in the flow*

There are alternative explanations for the striking appearance of POD modes for $k_x = 0$ which differ in spanwise wavenumber while exhibiting roll-streak structure (cf. Figs. 3 and 4). One interpretation of these structures is that they correspond to stable linear S3T modes that are maintained by excitation from random perturbations in the

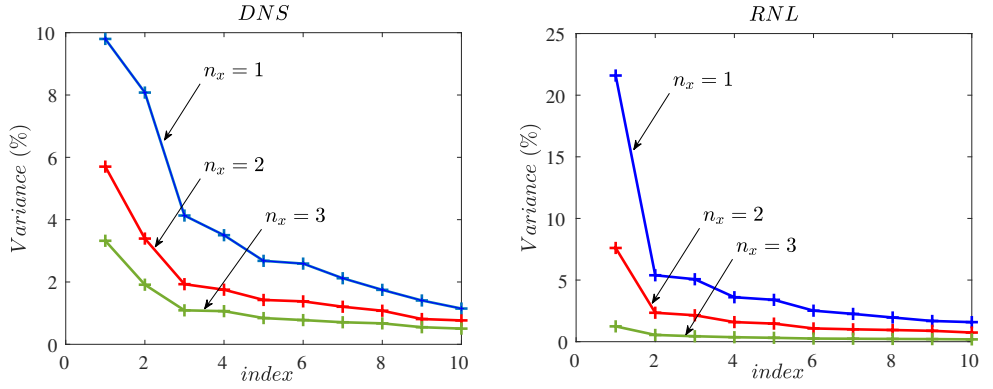

Figure 10: Percentage of energy density accounted for the POD modes as a function of the order of the mode (a) in NL100 and (b) in RNL100. POD's with streamwise Fourier component $n_x = 1$ are in blue; POD's with streamwise Fourier component $n_x = 2$ are in red; POD's with streamwise Fourier component $n_x = 3$ in green. The corresponding streamwise wavenumber is $k_x = 2\pi n_x/L_x$.

homogeneous background of turbulence. Due to the scale insensitivity of the roll-streak formation process, a spectral hierarchy of self-similar roll-streak structures are supported as modes by the turbulence as revealed by S3T (Farrell & Ioannou 2012). These roll-streak modes have different scales and damping rates and are therefore expected to be excited at different amplitudes. This interpretation of the POD's is appropriate in the case of the roll-streaks that emerge in pre-transitonal flows as discussed in Farrell *et al.* (2017*b*). Also in beta-plane turbulence one observes intermittent emergence of jets with structure corresponding to stochastically excited S3T modes, manifestations of which are referred to in observations as latent jets (Constantinou *et al.* 2014; Farrell & Ioannou 2019). In this interpretation of the POD modes with various spanwise wavenumber the POD's are identifying structures that are independently existing in the flow.

However, there is an alternative interpretation, which is that the dominant structure in the flow is the finite amplitude localized streak of Fig. 7. In this interpretation the POD's reflect the amplitude of the spanwise Fourier components of this structure rather than corresponding to structures with independent existence.

In order to determine which of these alternative explanations for the POD structure at $k_x = 0$ is correct we compare in Fig. 8 the amplitudes of the Fourier components of the streak with the amplitude of the POD with corresponding spanwise Fourier component and in Fig. 9 we plot the structure of the first three Fourier components obtained from spanwise Fourier analysis of the velocity components of the mean streak. The agreement shown in these figures leads us to conclude that the explanation of the POD spectrum arising from Fourier decomposition of the mean streak is correct.

5.2. *DNS and RNL POD modes of the streamwise-varying flow*

Representing POD modes for the $k_x \neq 0$ flow perturbations to the low speed streak of the DNS and RNL, shown in Fig. 7a,b, require allowing for the effect of symmetry

breaking in the spanwise by the low speed streak forming instability. This requires explicitly incorporating dependence on the coordinate z in the POD representation. We consider POD modes in the form:

$$\phi_{k_x} = \begin{pmatrix} \alpha_{k_x}(y,z) \\ \beta_{k_x}(y,z) \\ \gamma_{k_x}(y,z) \end{pmatrix} e^{ik_x x} \ , \tag{5.1}$$

with $\alpha_{k_x}(y,z)$,$\beta_{k_x}(y,z)$ and $\gamma_{k_x}(y,z)$ the components of the velocity of the POD in the streamwise, wall-normal and spanwise direction that determine the wall-normal and spanwise structure of the POD's. If the alignment of the data were not performed the data would be statistically homogeneous in both the x and z directions and the structure of the POD's would be by necessity constrained to be of the form $e^{i(k_x x + k_z z)}$ and would not reflect the localized structure of the perturbation fields about the streak. This is consistent with the interpretation of the POD modes given above: the $k_x = 0$ POD's reveal the spanwise Fourier components of the streak and not their phase. We note that projection of the $k_x = 0$ POD's on the streamwise mean structure recovered by collocation succeeded in identifying the phase of these spanwise harmonics and showing that they constitute Fourier components of the non-harmonic mean streak structure.

The flow field shown in Fig. 7 reveals a spanwise localized roll-streak structure symmetric about $z/h = \pi/2$. The perturbations in the far field have substantial variance and are approximately spanwise homogeneous. In order to isolate the streamwise-varying POD structures associated with the localized low-speed streak while avoiding contamination by the spanwise homogeneous far-field with harmonic structure we weight the data used to calculate the covariances C_{k_x} with a spatial filter that suppresses the variance in the far-field. We have chosen a Tukey filter in the interval $z = [0, \pi]$ with equation:

$$f(z) = \begin{cases} 1/2\left[1 + \cos\left(\pi/\delta\left((\pi - 2z)/\pi + (1-\delta)\right)\right)\right] \ , & (\pi - 2z)/\pi < \delta - 1, \\ 1 \ , & |(\pi - 2z)/\pi| \leqslant 1 - \delta \ , \\ 1/2\left[1 + \cos\left(\pi/\delta\left(((\pi - 2z)/\pi - (1-\delta)\right)\right)\right] \ , & (\pi - 2z)/\pi > 1 - \delta \ . \end{cases} \tag{5.2}$$

The parameter δ dictates the width of the filter and is chosen to sample the perturbation field in the vicinity of the streak. The values $\delta = 0.7$ and $\delta = 0.55$ are selected for NL100 and RNL100, respectively, since the RNL100 streak covers a wider area of the spanwise flow. The spanwise extent of the filter is indicated in the plots.

Eigen-decomposition of the covariance of perturbations from the streak structure was used to obtain the associated POD's for each streamwise Fourier component. The percentage of the total energy density accounted for by the first 10 POD's of the first three streamwise wavenumbers is plotted in Fig. 10a for NL100 and in Fig. 10b for RNL100.

Wall-normal velocity contours of the first two POD's of the NL100 simulation with streamwise Fourier component $n_x = 1$ are plotted in Fig. 11; similar contours for the second streamwise Fourier component, $n_x = 2$, are shown in Fig. 12. The similarity in structure and in orientation with the streamwise streak of these POD velocity components is clear. Consistent with the mirror symmetry of the streak in the spanwise direction these POD's are split between sinuous structure, with $u(x,y,z,t) = -u(x,y,-z,t)$, $v(x,y,z,t) = -v(x,y,-z,t)$ and $w(x,y,z,t) = w(x,y,-z,t)$, and varicose structure, with $u(x,y,z,t) = u(x,y,-z,t)$, $v(x,y,z,t) = v(x,y,-z,t)$ and $w(x,y,z,t) = -w(x,y,-z,t)$. The dominance of the top sinuous structure variance, shown in Fig 10a, indicates that it is preferentially expressed relative to the other components of the perturbation field.

The top RNL POD, which is also sinuous, and the top RNL varicose POD are similarly plotted at the wall-normal plane $y/h = 0.44$ in Fig. 13 and 14. It is again clear that a

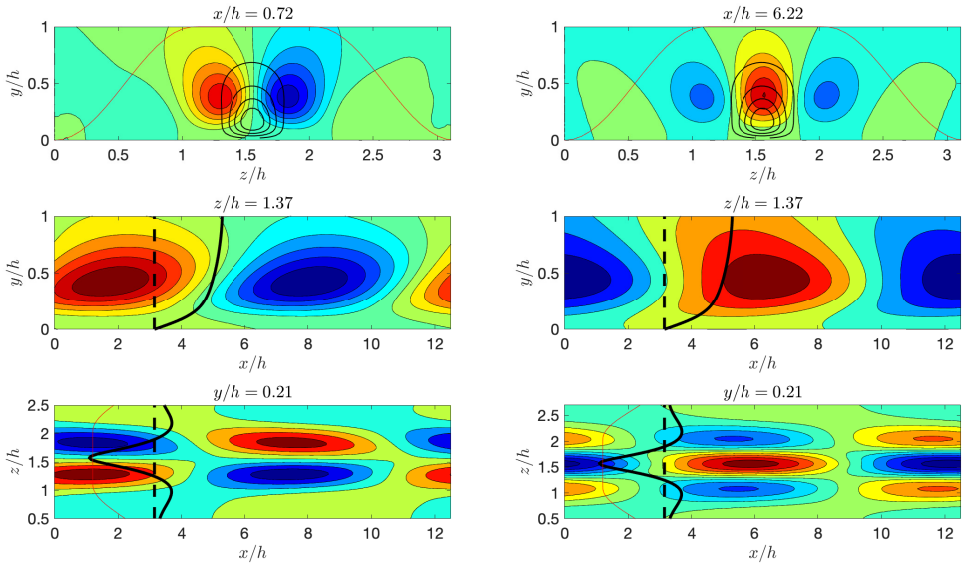

(a) (b)

Figure 11: For NL100: wall-normal velocity contour plots of the 1st and 2nd POD modes with streamwise Fourier component $n_x = 1$. At the top are shown contours of the wall normal velocity of the POD mode in the $y - z$ plane at a location in x; with the black contours indicating the shape of the underlying low-speed streak; the red line indicates the spanwise extent of the Tukey filter with $\delta = 0.7$ that has been applied to the perturbation field. At the center are shown contours of the wall normal velocity of the POD mode in the $x - y$ plane at $z/h = 1.37$, just off the center of the streak; the continuous black line indicates the shape of the mean flow at this section. At the bottom are shown contours of the wall normal velocity in the $z - x$ plane at $y/h = 0.21$, near the maximum of the low speed streak (cf. Fig. 6); the continuous black line indicates the shape of the mean flow at this section; the red line indicates the shape of the Tukey filter a) Left panels: the first POD has sinuous structure. b) Right panels: the second POD has varicose structure.

sinuous POD emerges as the component of highest variance associated with the streamwise streak, whereas the variance of the varicose $n_x = 1$ POD is suppressed below the second mode, which is also sinuous.

5.3. *Relation of the top $k_x \neq 0$ POD modes to structures of optimal growth on the streamwise-mean streak*

The striking structural similarity of the top POD modes associated with perturbations to the streamwise-mean streak in DNS and RNL suggests a common explanation for these POD's. Given that the streak is modally stable the default explanation is excitation of the optimally growing perturbation on the streamwise streak by the stochastic turbulent background velocity field.

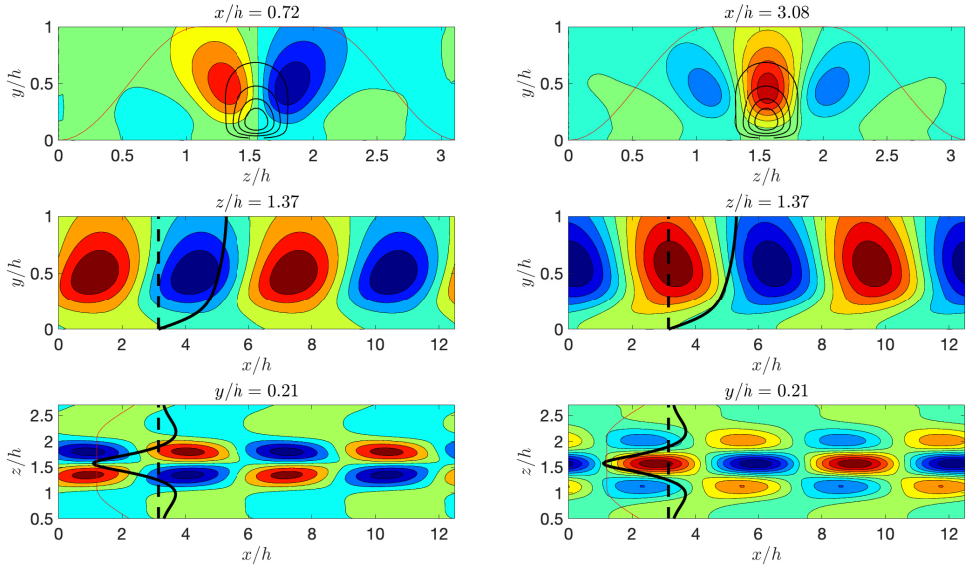

(a) (b)

Figure 12: For NL100: wall-normal velocity contour plots of the 1st and 2nd POD modes with streamwise Fourier component $n_x = 2$. The figure is structured as in Fig. 11. The first POD has sinuous structure, while the second POD has varicose structure.

Because the streamwise mean streak is mirror symmetric in the spanwise direction the optimal perturbations are also either sinuous or varicose. Indicative of the sinuous and varicose structure of the top two $n_x = 1$ optimal perturbations of the NL100 streamwise mean flow for optimizing time $T_{opt} = 5$ is shown in Fig. 15 at the time of their maximum energy. The corresponding optimals for the RNL100 streamwise mean flow are similar. The evolution of the energy of the two optimals shown in Fig. 17 for the NL100 and RNL100 streamwise-mean flows demonstrates the general property that in the presence of a mirror-symmetric streak the sinuous perturbations grow more than the varicose. This property is consistently reflected in the variance accounted for by the sinuous and varicose POD's as mean-perturbation energy transfer events in the turbulent flow are dominated by the non-normal growth of optimal perturbations. The transient growth of perturbations on the streak occur on shear time scales of 5-10 and would be expected if optimal growth explains the POD structure that the POD's should resemble the average structure of the 5-10 shear time optimals about the times of their energy maximum. In order to test this explanation for the observed POD structure shown in Fig. 11 are the first and second $n_x = 1$ POD's for NL100 and in Fig. 15 the associated first two $T_{opt} = 5$ shear time optimals at their times of largest energy growth. Similarly, in Fig. 16 are shown the $n_x = 1$ first two $T_{opt} = 5$ shear time optimals for RNL100 at their times of maximum energy growth, the first being sinuous and the second varicose. Comparison with the associated first and third POD shown in Fig. 13 reveals a clear resemblance of

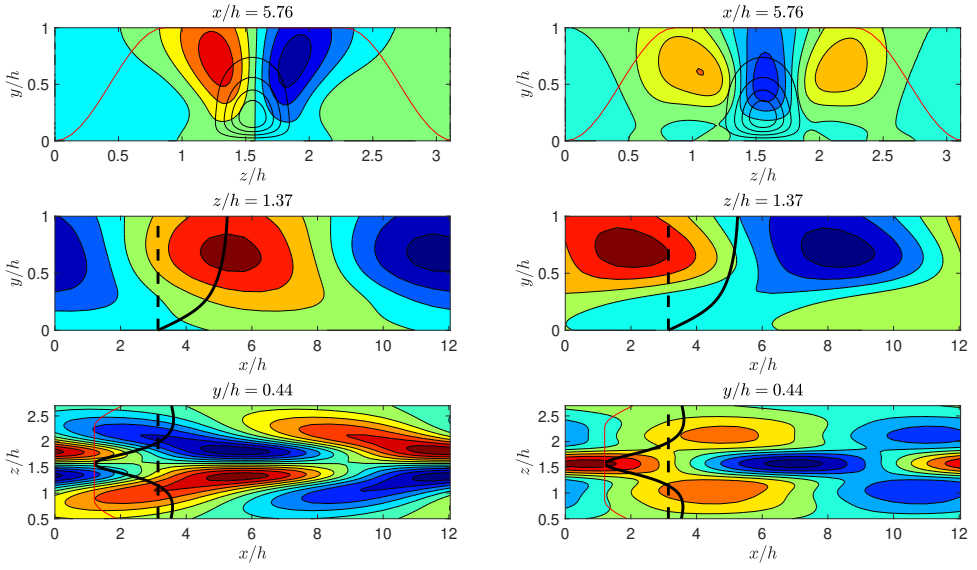

(a) (b)

Figure 13: For RNL100: wall-normal velocity contour plots of the 1st and 3rd POD modes with streamwise Fourier component $n_x = 1$. The first POD has sinuous structure, while the third POD has varicose structure. The second POD (not shown) has sinuous structure and is similar to the first POD.

these structures consistent with the existence of a causal association between POD's and underlying structures with optimal transient growth.

6. Discussion

POD analysis was carried out on a DNS of turbulent Poiseuille flow at $R = 1650$ and the corresponding quasi-linear RNL simulation. The POD's analyzed were chosen to correspond to the two variables of the S3T SSD, the streamwise-mean flow and the covariance of perturbations from it, for which analytical solution for the dynamics of the turbulence is known. The RNL system was chosen for this comparison because it is dynamically similar to S3T so that the DNS/RNL/S3T form a conceptual bridge connecting the analytically comprehensive characterization of turbulence in S3T to DNS turbulence, which lacks a similarly complete analytic characterization. The motivation for this work was to explore the extent to which DNS turbulence has dynamics consistent with the analytically characterized turbulence of the S3T SSD.

Considering first the streamwise-mean component of the turbulence, striking resemblance between the velocity fields corresponding to the roll-streak at $k_x = 0$ were seen in the two simulations. This similarity strongly suggests that the scale invariant roll-streak formation mechanism identified in the S3T SSD is also operating in DNS. To complete

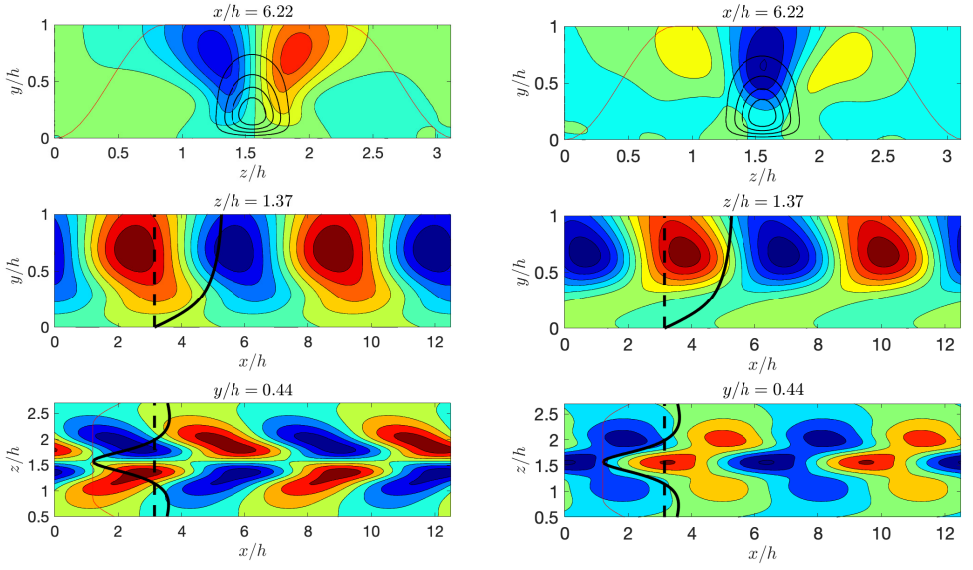

Figure 14: For RNL100: wall-normal velocity contour plots of the 1st and 2nd POD modes with streamwise Fourier component $n_x = 2$. The first POD has sinuous structure, while the second POD has varicose structure.

this identification the second component of the S3T SSD, which is the perturbation covariance, was examined. To this end the perturbation structures collocated with the streak were investigated in the RNL and DNS. In order to isolate the POD's of the $k_x \neq 0$ perturbations that are associated with the roll-streak structure, the velocity fields were translated to center the dominant low speed streak at the spanwise center of the channel. POD analysis of the aligned velocity fields revealed that the perturbation covariance is associated with strikingly similar structures in DNS and RNL . These structures resemble the oblique waves that had previously been identified in analysis of the S3T SSD with the Reynolds stress arising from optimal perturbations that forces the roll that supports the steak through the lift-up process (Farrell & Ioannou 2012).

In this work we have provided evidence using POD analysis that the roll-streak SSP operating in RNL turbulence is the same as that operating in DNS. Because the mechanism maintaining turbulence in the S3T/RNL system has been comprehensively characterized (Farrell & Ioannou 2012; Thomas *et al.* 2014, 2015; Farrell *et al.* 2016, 2017*a*), this close correspondence between the dominant structures in RNL and DNS and the fact that the RNL has the same dynamical restriction as the S3T SSD and is analytically similarly characterized argues that the roll-streak lift-up mechanism known to be operating at $k_x = 0$ in RNL and in the S3T SSD is the same dynamically as that operating in DNS.

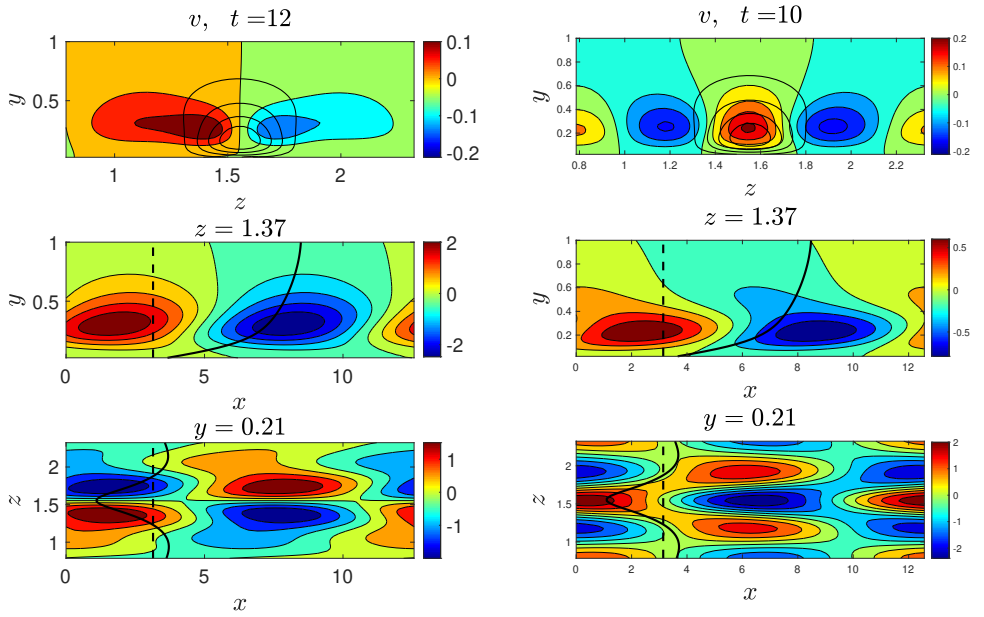

(a) (b)

Figure 15: Wall-normal velocity contours of the 1st and 2nd optimal perturbation with streamwise Fourier component $n_x = 1$ for optimizing time $T_{opt} = 5$ of the NL100 streamwise-mean streamwise velocity shown in Fig. 7a. The figure is structured as in Fig. 11 a) Left panels: the first optimal has sinuous structure with energy growth at T_{opt} of 28 and is shown at $t = 12.5$ when its energy growth is 55. b) Right panels: the second optimal has varicose structure with energy growth at T_{opt} of 23 and is shown at $t = 10$ when its energy growth is 32.5. The evolution of their energy density is shown in Fig. 17a.

Acknowledgments

This work was funded in part by the Second Multiflow Program of the European Research Council. Marios-Andreas Nikolaidis gratefully acknowledges the support of the Hellenic Foundation for Research and Innovation (HFRI) and the General Secretariat for Research and Technology (GSRT), under the HFRI PhD Fellowship grant 1718/14518. Brian F. Farrell was partially supported by NSF AGS-1640989. We would like to thank Dennice Gayme, Daniel Chung and Navid Constantinou for their helpful comments.

Declaration of interest

The authors report no conflict of interest

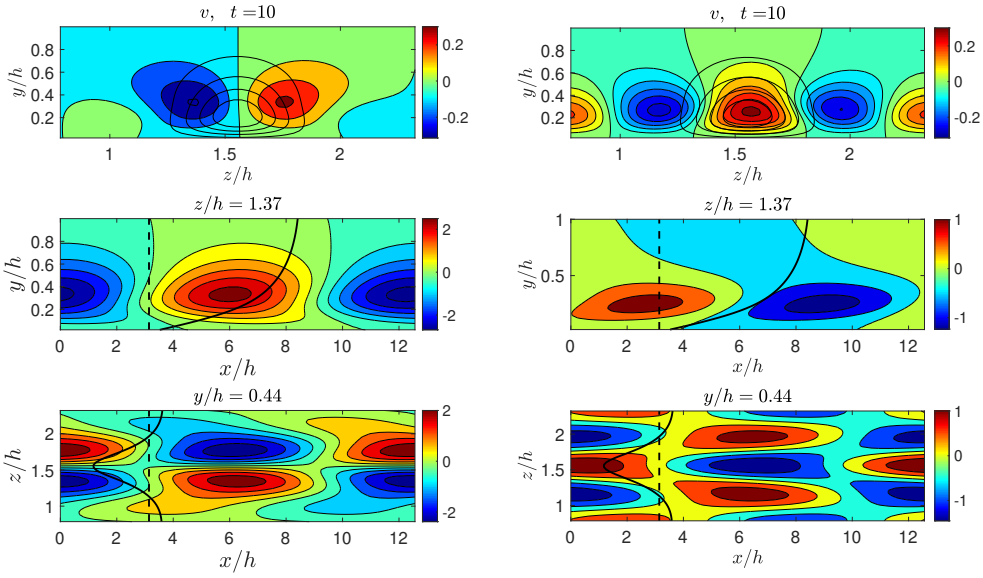

(a) (b)

Figure 16: Wall-normal velocity contours of the 1st and 2nd optimal perturbation with streamwise Fourier component $n_x = 1$ for optimizing time $T_{opt} = 5$ of the RNL100 streamwise-mean streamwise velocity shown in Fig. 7b. The figure is structured as in Fig. 11 a) Left panels: the first optimal has sinuous structure with energy growth at T_{opt} of 33 and is shown at $t = 10$ when its energy growth is 68. b) Right panels: the second optimal has varicose structure with energy growth at T_{opt} of 29 and is shown at $t = 10$ when its energy growth is 47. The evolution of their energy density is shown in Fig. 17b.

Appendix A. Construction of the covariances with symmetry restrictions

Homogeneity in the streamwise and spanwise directions allows the decomposition of velocity field snapshots into sums of plane waves with Fourier coefficients that depend on the wall-normal direction. Application of mirror symmetries in y and z incorporates the 2-point statistics from the total flow field into a single covariance for each $|k_x|, |k_z|$ wavenumber pair. Convergence towards these statistical symmetries is slow. For example in Fig. 18 we demonstrate the slow convergence of the statistics to the asymptotic mirror symmetric state about the wall-normal plane at the center of the channel.

For a single k_z, k_x pair the three components of the velocity field is comprised by two independent plane waves

$$\Phi_{k_x} e^{ik_x x} = \begin{pmatrix} A_{k_x,k_z}(y) \\ B_{k_x,k_z}(y) \\ \Gamma_{k_x,k_z}(y) \end{pmatrix} e^{i(k_x x + k_z z)} + \begin{pmatrix} A_{k_x,-k_z}(y) \\ B_{k_x,-k_z}(y) \\ \Gamma_{k_x,-k_z}(y) \end{pmatrix} e^{i(k_x x - k_z z)} \,. \qquad \text{(A 1)}$$

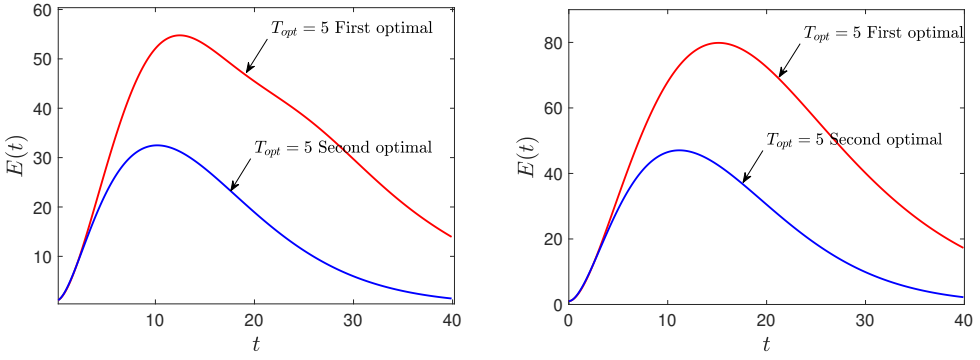

(a) (b)

Figure 17: Evolution of the energy of the $T_{opt} = 5$ optimals with $n_x = 1$ and unit initial energy density. The first optimal has sinuous structure and the second varicose. a) Left panel: for the DNS streamwise mean flow streamwise velocity shown in Fig. 7a, which is hydrodynamically stable with the least damped mode decaying at $\sigma = -0.014$. a) Right panel: for the RNL streamwise mean flow streamwise velocity shown in Fig. 7b, which is hydrodynamically stable with the least damped mode decaying at $\sigma = -0.004$.

With A we denote the streamwise component of the velocity field, B the wall-normal and with Γ the spanwise component. A special case is the $k_x = 0$ component for which the coefficients of k_z and $-k_z$ will be complex conjugates. The two symmetries we consider are mirror symmetry in y with respect to the half-channel $x - z$ plane at $y = 1$ and in z with respect to the half width plane $x - y$ at $z = \pi/2$. Those produce a fourfold increase in the amount of data that will be included in the covariance matrix.

First we consider the spanwise mirroring operation. This will transform z to $\pi - z$ and change sign in the spanwise velocity component.

$$\hat{S}_z \Phi_{k_x} e^{ik_x x} = \begin{pmatrix} A_{k_x,-k_z}(y) \\ B_{k_x,-k_z}(y) \\ -\Gamma_{k_x,-k_z}(y) \end{pmatrix} e^{i(k_x x + k_z(z-\pi))} + \begin{pmatrix} A_{k_x,k_z}(y) \\ B_{k_x,k_z}(y) \\ -\Gamma_{k_x,k_z}(y) \end{pmatrix} e^{i(k_x x - k_z(z-\pi))} \quad \text{(A 2)}$$

The $-ik_z\pi$ phase that appears in the plane wave will cancel out when the covariance is formed.

In the wall-normal mirroring the effect is to transform y to $2 - y$ and change sign in the wall-normal velocity component,

$$\hat{S}_y \Phi_{k_x} e^{ik_x x} = \begin{pmatrix} A_{k_x,k_z}(2-y) \\ -B_{k_x,k_z}(2-y) \\ \Gamma_{k_x,k_z}(2-y) \end{pmatrix} e^{i(k_x x + k_z z)} + \begin{pmatrix} A_{k_x,-k_z}(2-y) \\ -B_{k_x,-k_z}(2-y) \\ \Gamma_{k_x,-k_z}(2-y) \end{pmatrix} e^{i(k_x x - k_z z)} \quad \text{(A 3)}$$

What the $2 - y$ coordinate implies is that the wall-normal structure will be inverted for each component. Summarizing the above operations, the total covariance will be comprised by the individual covariances obtained for each of the 4 components below

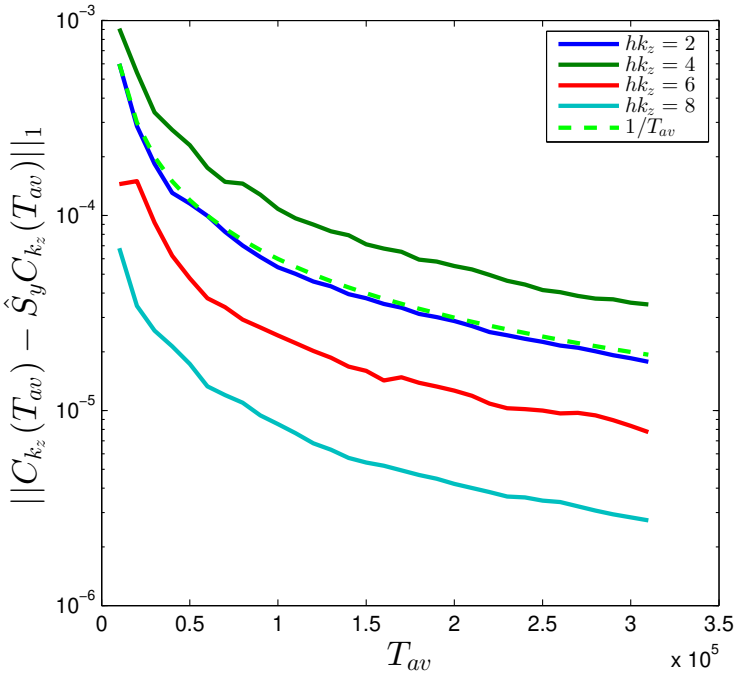

Figure 18: The 1-norm of the difference $C_{k_z} - \hat{S}_y C_{k_z}$ between the covariance matrix C_{k_z} (4.2), and the covariance of the reflected flow about the $x-z$ plane at the center of the flow ($y = 1$) as a function of the averaging time, T_{av}, for $hk_z = 2, 4, 6, 8$ for a DNS of NL100. $\hat{S}_y$ is defined in Appendix A, Eq. (A 8). This plot verifies that reflection symmetry about the centerline is a statistical symmetry of the flow and that this symmetry is approached at the rate $1/T_{av}$ consistent with the law of large numbers for quadratic statistics. Time is non-dimensionalized by h/U.

$$\Phi_{k_z} = \begin{pmatrix} A_{k_z}(y) \\ B_{k_z}(y) \\ \Gamma_{k_z}(y) \end{pmatrix} e^{ik_z z} \,, \hat{S}_z \Phi_{k_z} = \begin{pmatrix} A_{-k_z}(y) \\ B_{-k_z}(y) \\ -\Gamma_{-k_z}(y) \end{pmatrix} e^{ik_z z} \,,$$

$$\hat{S}_y \Phi_{k_z} = \begin{pmatrix} A_{k_z}(2-y) \\ -B_{k_z}(2-y) \\ \Gamma_{k_z}(2-y) \end{pmatrix} e^{ik_z z} \,, \hat{S}_z \hat{S}_y \Phi_{k_z} = \begin{pmatrix} A_{-k_z}(2-y) \\ -B_{-k_z}(2-y) \\ -\Gamma_{-k_z}(2-y) \end{pmatrix} e^{ik_z z} \,, \quad \text{(A 4)}$$

where the k_x subscript has been omitted.

We form the covariance obtained from the initial wave. To highlight the inner structure of this covariance due to the different velocity components the following representation is chosen

$$C_{k_z} = \begin{pmatrix} C^{uu}_{k_z} & C^{uv}_{k_z} & C^{uw}_{k_z} \\ C^{vu}_{k_z} & C^{vv}_{k_z} & C^{vw}_{k_z} \\ C^{wu}_{k_z} & C^{wv}_{k_z} & C^{ww}_{k_z} \end{pmatrix} \,, \quad \text{(A 5)}$$

with $C^{u_i u_j}_{k_z} = (C^{u_j u_i}_{k_z})^\dagger$. In the following the k_z subscript will be omitted where possible

and instead of $u_i u_j$ the superscript ij will be used. So the covariance can be written as:

$$C = \begin{pmatrix} C^{11} & C^{12} & C^{13} \\ C^{21} & C^{22} & C^{23} \\ C^{31} & C^{32} & C^{33} \end{pmatrix} . \tag{A 6}$$

Statistical symmetry in reflections of the velocities in z merge the covariance of the $-k_z$ component with the k_z. The negative k_z covariance will be modified to account for this symmetry

$$\hat{S}_z C_{-k_z} = \begin{pmatrix} (C^{11}) & (C^{12}) & -(C^{13}) \\ (C^{21}) & (C^{22}) & -(C^{23}) \\ -(C^{31}) & -(C^{32}) & (C^{33}) \end{pmatrix} . \tag{A 7}$$

Reflections in y require to reverse the order of the row and column indexes in each individual covariance and if this operation is noted as $\hat{S}_y C^{ij} = C_R^{ij}$ we have:

$$\hat{S}_y C = \begin{pmatrix} C_R^{11} & -C_R^{12} & C_R^{13} \\ -C_R^{21} & C_R^{22} & -C_R^{23} \\ C_R^{31} & -C_R^{32} & C_R^{33} \end{pmatrix} . \tag{A 8}$$

The total covariance will be comprised by the following components

$$C^t_{k_z} = (C_{k_z} + \hat{S}_y C_{k_z} + \hat{S}_z C_{-k_z} + \hat{S}_y \hat{S}_z C_{-k_z})/4 \tag{A 9}$$

To account correctly for the relative energy between $k_z = 0$ and $k_z \neq 0$ components the eigenvalues of covariances with $k_z \neq 0$ are doubled in the ordering process.

REFERENCES

Aubry, Nadine, Holmes, Philip, Lumley, John L. & Stone, Emily 1988 The dynamics of coherent structures in the wall region of a turbulent boundary layer. *Journal of Fluid Mechanics* **192**, 115–173.

Avsarkisov, V., Hoyas, S., Oberlack, M. & Garcia-Galache, J. P. 2014 Turbulent plane Couette flow at moderately high Reynolds number. *J. Fluid Mech.* **751**, R1.

Berkooz, G., Holmes, P. & Lumley, J. L. 1993 The proper orthogonal decomposition in the analysis of turbulent flows. *Annu. Rev. Fluid Mech.* **25** (1), 539–575.

Bretheim, J. U., Meneveau, C. & Gayme, D. F. 2015 Standard logarithmic mean velocity distribution in a band-limited restricted nonlinear model of turbulent flow in a half-channel. *Phys. Fluids* **27**, 011702.

Chernyshenko, S. I. & Baig, M. F. 2005 The mechanism of streak formation in near-wall turbulence. *Journal of Fluid Mechanics* **544**, 99–131.

Constantinou, N. C., Farrell, B. F. & Ioannou, P. J. 2014 Emergence and equilibration of jets in beta-plane turbulence: applications of Stochastic Structural Stability Theory. *J. Atmos. Sci.* **71** (5), 1818–1842.

Farrell, B. F., Gayme, D. F. & Ioannou, P. J. 2017*a* A statistical state dynamics approach to wall-turbulence. *Phil. Trans. R. Soc. A* **375** (2089), 20160081.

Farrell, B. F. & Ioannou, P. J. 1993 Stochastic forcing of the linearized Navier-Stokes equations. *Phys. Fluids A* **5**, 2600–2609.

Farrell, B. F. & Ioannou, P. J. 2001 Accurate low-dimensional approximation of the linear dynamics of fluid flow. *J. Atmos. Sci.* **58** (18), 2771–2789.

Farrell, B. F. & Ioannou, P. J. 2012 Dynamics of streamwise rolls and streaks in turbulent wall-bounded shear flow. *J. Fluid Mech.* **708**, 149–196.

Farrell, B. F. & Ioannou, P. J. 2017 Statistical state dynamics-based analysis of the physical mechanisms sustaining and regulating turbulence in Couette flow. *Phys. Rev. Fluids* **2** (8), 084608.

Farrell, B. F. & Ioannou, P. J. 2019 Statistical State Dynamics: A new perspective on turbulence in shear flow. In *Zonal jets: Phenomenology, genesis, and physics* (ed. B. Galperin & P. L. Read), chap. 25, pp. 380–400. Cambridge University Press.

Farrell, B. F., Ioannou, P. J., Jiménez, J., Constantinou, N. C., Lozano-Durán, A. & Nikolaidis, M.-A. 2016 A statistical state dynamics-based study of the structure and mechanism of large-scale motions in plane Poiseuille flow. *J. Fluid Mech.* **809**, 290–315.

Farrell, B. F., Ioannou, P. J. & Nikolaidis, M.-A. 2017*b* Instability of the roll–streak structure induced by background turbulence in pretransitional Couette flow. *Phys. Rev. Fluids* **2** (3), 034607.

Farrell, B. F., Ioannou, P. J. & Nikolaidis, M.-A. 2018 Statistical State Dynamics based study of the role of nonlinearity in the maintenance of turbulence in Couette flow. *Phys. Rev. Fluids* (submitted, arXiv:1808.07948).

Hamilton, K., Kim, J. & Waleffe, F. 1995 Regeneration mechanisms of near-wall turbulence structures. *J. Fluid Mech.* **287**, 317–348.

Hellström & Smits, A. J. 2017 Structure identification in pipe flow using proper orthogonal decompositionvisualizing the very-large-scale motions in turbulent pipe flow. *Phil. Trans. R. Soc. A* **375**, 20160086.

Hellström, L. H. O., Sinha, A. & Smits, A. J. 2011 Visualizing the very-large-scale motions in turbulent pipe flow. *Phys. Fluids* **23**, 011703.

Hwang, Y. & Cossu, C. 2010 Self-sustained process at large scales in turbulent channel flow. *Phys. Rev. Lett.* **105**, 044505.

Hwang, Y. & Cossu, C. 2011 Self-sustained processes in the logarithmic layer of turbulent channel flows. *Phys. Fluids* **23**, 061702.

Hwang, Yongyun, Willis, Ashley P. & Cossu, Carlo 2016 Invariant solutions of minimal large-scale structures in turbulent channel flow for Re_τ up to 1000. *Journal of Fluid Mechanics* **802**, R1.

Jiménez, J. & Moin, P. 1991 The minimal flow unit in near-wall turbulence. *J. Fluid Mech.* **225**, 213–240.

Jiménez, J. & Pinelli, A. 1999 The autonomous cycle of near-wall turbulence. *J. Fluid Mech.* **389**, 335–359.

Kawahara, G. & Kida, S. 2001 Periodic motion embedded in plane Couette turbulence: regeneration cycle and burst. *J. Fluid Mech.* **449**, 291–300.

Kim, J., Moin, P. & Moser, R. 1987 Turbulence statistics in fully developed channel flow at low Reynolds number. *J. Fluid Mech.* **177**, 133–166.

Lozano-Durán, Adrián, Constantinou, Navid C., Nikolaidis, Marios-Andreas & Karp, Michael 2021 Cause-and-effect of linear mechanisms sustaining wall turbulence. *Journal of Fluid Mechanics* **914**, A8.

Lumley, J. L. 1967 The structure of inhomogeneous turbulence. In *Atmospheric Turbulence and Radio Wave Propagation* (ed. A. M. Yaglom & V. I. Tatarskii), pp. 166–178. Nauka, Moscow.

Moehlis, J., Smith, T. R., Holmes, P. & Faisst, H. 2002 Models for turbulent plane Couette flow using the proper orthogonal decomposition. *Phys. Fluids* **14**, 2493–2507.

Moin, P. & Moser, R. D. 1989 Characteristic-eddy decomposition of turbulence in a channel. *J. Fluid Mech.* **200**, 471–509.

Nikolaidis, M.-A. & Ioannou, P. J. 2021 Synchronization of Low Reynolds Number Plane Couette Turbulence. *J. Fluid Mech.* **(submitted)**.

Rowley, C. W. 2005 Model reduction for fluids, using balanced proper orthogonal decomposition. *International Journal of Bifurcation and Chaos* **15** (03), 997–1013.

Schoppa, W. & Hussain, F. 2002 Coherent structure generation in near-wall turbulence. *J. Fluid Mech.* **453**, 57–108.

Sirovich, L., Ball, K. S. & Keefe, L. R. 1990 Plane waves and structures in turbulent channel flow. *Phys. Fluids A* **2**, 2217–2226.

Thomas, V., Farrell, B. F., Ioannou, P. J. & Gayme, D. F. 2015 A minimal model of self-sustaining turbulence. *Phys. Fluids* **27**, 105104.

Thomas, V., Lieu, B. K., Jovanović, M. R., Farrell, B. F., Ioannou, P. J. & Gayme, D. F. 2014 Self-sustaining turbulence in a restricted nonlinear model of plane Couette flow. *Phys. Fluids* **26**, 105112.

Waleffe, F. 1997 On a self-sustaining process in shear flows. *Phys. Fluids* **9**, 883–900.
Waleffe, F. 2003 Homotopy of exact coherent structures in plane shear flows. *Phys. Fluids* **15**, 1517–1534.